Machine-Learning-Guided Prediction Models of Critical Temperature of Cuprates

Dongeon Lee[1], Daegun You[2], Dongwoo Lee[2], Xin Li[3], and Sooran Kim[1*]

[1]Department of Physics Education, Kyungpook National University, Daegu 41566, South Korea

[2]School of Mechanical Engineering, Sungkyunkwan University, Suwon, Gyeonggi-do 16419, South Korea

[3]John A. Paulson School of Engineering and Applied Sciences, Harvard University, Cambridge, Massachusetts 02138, United States

*Corresponding author: sooran@knu.ac.kr

1. Computational details and data acquisition

All density functional theory (DFT) calculations were performed with the Vienna Ab initio Simulation Package (VASP) implementing the plane-wave pseudopotential method[1]. PAW-PBE functional was used for the exchange-correlation functional[2]. We performed non-spin polarized calculations Cu correlation with U = 8 eV and J = 1.34 eV for the correlated d bands of Cu[3]. A 520 eV plane-wave energy cutoff was used. Atomic positions are relaxed from initial experimental structures from the inorganic crystal structure database (ICSD). We fully relaxed the hypothetical structures including atomic positions and lattice parameters. To calculate the forces on an apical cation and apical oxygen, we manually distorted the apical oxygen toward the CuO_2 layer by 0.12 Å.

29 hole-doped cuprates are collected for the dataset including representative 19 cuprates from Kim *et al.*[4], $LuBa_2Cu_3O_7$, $ErBa_2Cu_3O_7$, $HoBa_2Cu_3O_7$, $GdBa_2Cu_3O_7$, $SmBa_2Cu_3O_7$, Hg-1234, Hg-1245, Hg-1256, Bi-2234, and Tl-2234. Abbreviations, experimental $T_{c,max}$, and apical oxygen height of each material are summarized in Table S1. The statistic information of input $T_{c,max}$ for the prediction model are 32 K (min), 135 K (max), 93.7 K (mean), and 25.9 K (standard deviation). We select four features, which have been reported as material dependent parameters in previous studies[4,5]: the Bader charge of the apical oxygen (B), the apical force (F_A), the number of CuO_2 layers (L), and apical oxygen height (d_A). The definition of the apical force is the average of the absolute value of apical oxygen and apical cation, which is connected to the bond strength between apical atoms. Among four features, F_A and B are easily collected from DFT calculations without demanding high computational cost while L and d_A are readily accessible structural information.

2. Machine learning algorithms

We employed two machine learning (ML) algorithms: one is a parametric BFS model[6–9] and another is a nonparametric random forest (RF) regression model[10]. All machine learning algorithms were developed using the *scikit-learn* python library[11]. To avoid overfitting, we evaluated the performance of each model using leave-one-out cross-validation (LOOCV), which splits N data into different N subsets (i.e. N-1 training and 1 test datasets) and averages evaluation error over all splits. The root-mean-square-error (RMSE) and the coefficient of determination (R^2) are used to evaluate the accuracy of models.

The BFS model is a linear regression with various functional forms of features, which allow considering nonlinear relationships by converting primary features to the nonlinear functional forms of compound features. It has the advantage of providing the analytical functional relation between output and features.

We have four primary features (B, F_A, L, d_A) and considered 15 functions, $1, x, \frac{1}{x}, x^2, \frac{1}{x^2}, x^3, \frac{1}{x^3}, \sqrt{x}, \frac{1}{\sqrt{x}}, e^x, \frac{1}{e^x}, e^{1/x}, \frac{1}{e^{1/x}}, \ln(x+1), \frac{1}{\ln(x+1)}$ following previous BFS models[6,7,9]. The functional form of $\ln(x+1)$ was selected instead $\ln(x)$ to avoid the infinity from $1/\ln(x)$. These functions and primary features produce 57 prototypical features (i.e $\frac{1}{B}, \sqrt{F_A}$, etc). Multiplication of these prototypical features taken either two, three, or four generate 50,625 compound features. (i.e., $\frac{B}{\sqrt{F_A}}, \frac{L^3\sqrt{F_A}}{\ln(B+1)}, \frac{B^3 d_A^2}{\sqrt{F_A}\ln(L+1)}$, etc.)

We construct the linear regression models in the form of $T_{c,max} = \theta_0 + \theta_1 f_1$ (1C model), $T_{c,max} = \theta_0 + \theta_1 f_1 + \theta_2 f_2$ (2C model), $T_{c,max} = \theta_0 + \theta_1 f_1 + \theta_2 f_2 + \theta_3 f_3$ (3C model) using the compound features, f_x (x=1, 2, 3). We define mCnF model as a linear regression model with m compound features where each compound feature consists of n primary features. Note that each

compound feature in a *m*C*n*F model can have different *n* primary features. One example of a 3C2F model is $\theta_0 + \theta_1 \frac{e^B}{e^L} + \theta_2 \frac{1}{\sqrt{F_A}L} + \theta_3 \frac{e^{\frac{1}{L}}}{d_A}$. We searched the best BFS fit using all data as a training set and evaluated the three best-fit BFS models for each case using the LOOCV.

The RF is one of the most widely used ML methods due to its simplicity and ability to learn non-linear dependencies. The forest consists of multiple decision trees, where each tree is a non-parametric supervised learning method. This ensemble learning method does not require a scale of data and provides an accurate and stable prediction. Furthermore, we can estimate the importance of each feature, for example, using Gini importance (GI). The GI provides the quantitative contribution of each feature to an output parameter. As hyperparameters, the number of trees in the forest is 1000, and the number of features to consider when looking for the best split is a square root of number of features.

3. Summary of $T_{c,max}$, d_A, and abbreviation

Table S1. Summary of $T_{c,max}$, d_A, and abbreviation of each material. *d_A of YBCO6.5 is the averaged value below empty and filled CuO chains.

Chemical formula	$T_{c,max}$ (K)	d_A (Å)	Abbreviation	Family
La_2CuO_4	38[12]	2.412[13]	La214	La
$La_2CaCu_2O_6$	55[14]	2.309[15]		
$Pb_2Sr_2Cu_2O_6$	32[16]	2.350[16]		
$Pb_2Sr_2YCu_3O_8$	70[17]	2.238[17]		
YBa2Cu3O$_7$	93[18]	2.296[19]	YBCO7	Y
$YBa_2Cu_3O_{6.5}$	93	2.368*[20]	YBCO6.5	
$YBa_2Cu_3O_6$	93	2.466[19]	YBCO6	
$LaBa_2Cu_3O_7$	98.5[21]	2.165[22]		
$NdBa_2Cu_3O_7$	96[23]	2.247[22]		
$DyBa_2Cu_3O_7$	92[24]	2.269[22]		
$LuBa_2Cu_3O_7$	90[25]	2.369[26]		
$ErBa_2Cu_3O_7$	92[18]	2.293[27]		
$HoBa_2Cu_3O_7$	92[28]	2.230[29]		
$GdBa_2Cu_3O_7$	93.5[30]	2.260[31]		
$SmBa_2Cu_3O_7$	94.5[32]	2.258[31]		
$Bi_2Sr_2CuO_6$	40[33]	2.589[34]	Bi-2201	Bi
$Bi_2Sr_2CaCu_2O_8$	93[35]	2.509[36]	Bi-2212	
$Bi_2Sr_2Ca_2Cu_3O_{10}$	110[18]	2.528[37]	Bi-2223	
$Bi_2Sr_2Ca_3Cu_4O_{12}$	110[38]	2.616[39]	Bi-2234	
$Tl_2Ba_2CuO_6$	87[40]	2.714[34]	Tl-2201	Tl
$Tl_2Ba_2CaCu_2O_8$	110[40]	2.700[41]	Tl-2212	
$Tl_2Ba_2Ca_2Cu_3O_{10}$	125[42]	2.740[43]	Tl-2223	
$Tl_2Sr_2Ca_3Cu_4O_{12}$	119[44]	2.658[45]	Tl-2234	
$HgBa_2CuO_4$	94[46]	2.795[46]	Hg-1201	Hg
$HgBa_2CaCu_2O_6$	127[47]	2.787[48]	Hg-1212	
$HgBa_2Ca_2Cu_3O_8$	135[48]	2.748[48]	Hg-1223	
$HgBa_2Ca_3Cu_4O_{10}$	127[49]	2.816[50]	Hg-1234	
$HgBa_2Ca_4Cu_5O_{12}$	110[49]	2.827[51]	Hg-1245	
$HgBa_2Ca_5Cu_6O_{14}$	107[49]	2.761[51]	Hg-1256	

4. The shape of the equations of the best three 3C2F models

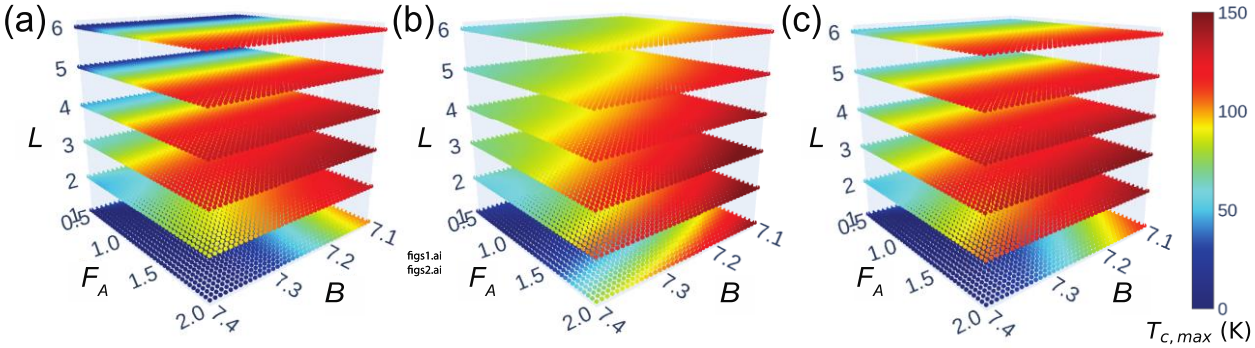

Figure S1. The shape of the equation from the 3C2F models with the RMSE of (a) 3.705 K (b) 3.795 K, and (c) 4.197 K. The color bar indicates the calculated $T_{c,max}$.

Figure S1 shows the shape of the BFS equations of the best three in the 3C2F model. Despite the different forms of the equations, general shapes of the equations are similar with common aspects of (i) smaller B for higher $T_{c,max}$, (ii) larger F_A for higher $T_{c,max}$, and (iii) maximum $T_{c,max}$ at L of 3 or 4.

5. Results of the 2C3F model

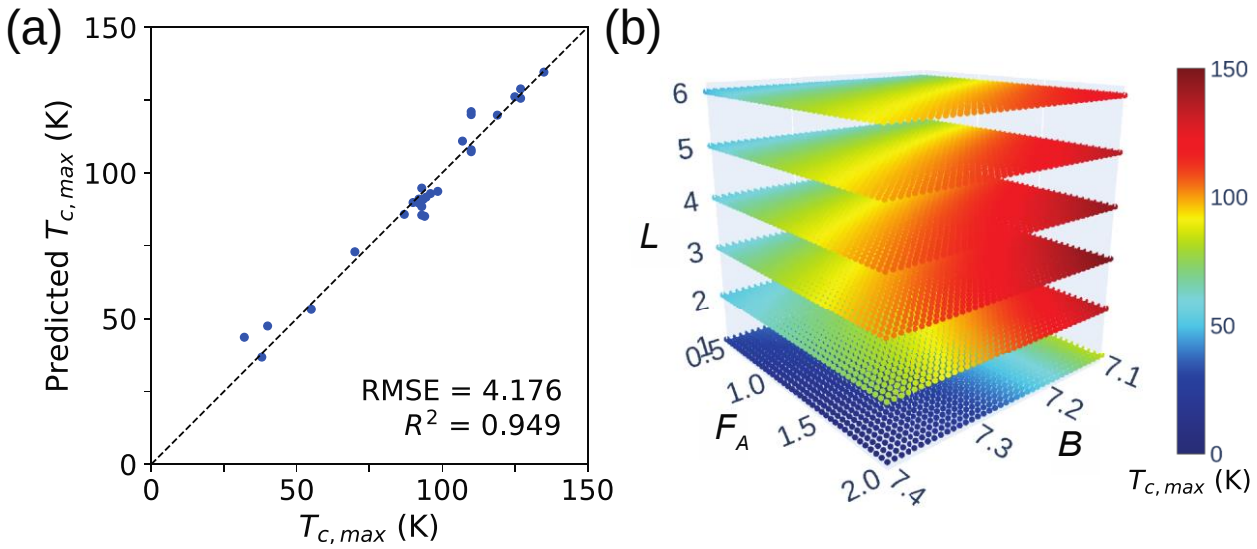

Figure S2. Performance of the 2C3F model. (a) Comparison of the experimental $T_{c,max}$ against the predicted $T_{c,max}$ obtained by the best 2C3F model. (b) The shape of the equation of the best 2C3F model with an averaged d_A of 2.494 Å of the dataset.

Figure S2 (a) shows the comparison of experimental $T_{c,max}$ and the best 2C3F model with the RMSE of 4.176 K and R^2 of 0.949. The best model of the 2C3F is comparable to the best model of the 3C2F with the RMSE of 3.705 K and R^2 of 0.969.

The equations in the best three 2C3F models exhibit the common form, $\frac{\sqrt{F_A}}{e^B\sqrt{L}}$ and $\frac{\ln(F_A+1)}{e^L}$ as shown in Table S2. The differences among them are $\frac{1}{\ln(d_A+1)}$, $\frac{1}{\sqrt{d_A}}$, and $\frac{1}{d_A}$, which monotonously decrease as increasing the d_A. Therefore, the equations share characteristics that increase of $T_{c,max}$ as (i) the B decreases, (ii) the F_A increases, (iii) the d_A increase, and (iv) maximum $T_{c,max}$ at L of 3 or 4. Figure S2 (b) illustrates the shape of the equation of the best 2C3F model as a representative. Since the equation of the 2C3F models has four parameters we fixed the d_A with the averaged value of 2.494 Å of the dataset for visualization.

Table S2. Details of model equations of the best three 2C3F models. F_A, B, L, and d_A represent the apical force, the Bader charge of the apical oxygen, the number of CuO_2 layers, and the apical oxygen height, respectively.

	Model equation	RMSE (K)	R^2
1	$-0.315 + 270\,\frac{10^3\sqrt{F_A}}{e^B\sqrt{L}} - 713\,\frac{\ln(F_A+1)}{e^L\ln(d_A+1)}$	4.176	0.949
2	$-2.16 + 273\,\frac{10^3\sqrt{F_A}}{e^B\sqrt{L}} - 905\,\frac{\ln(F_A+1)}{e^L\sqrt{d_A}}$	4.179	0.948
3	$11.3 + 246\,\frac{10^3\sqrt{F_A}}{e^B\sqrt{L}} - 1370\,\frac{\ln(F_A+1)}{e^L d_A}$	4.363	0.951

6. Predicted $T_{c,max}$ of hypothetical structures in the 2C3F model

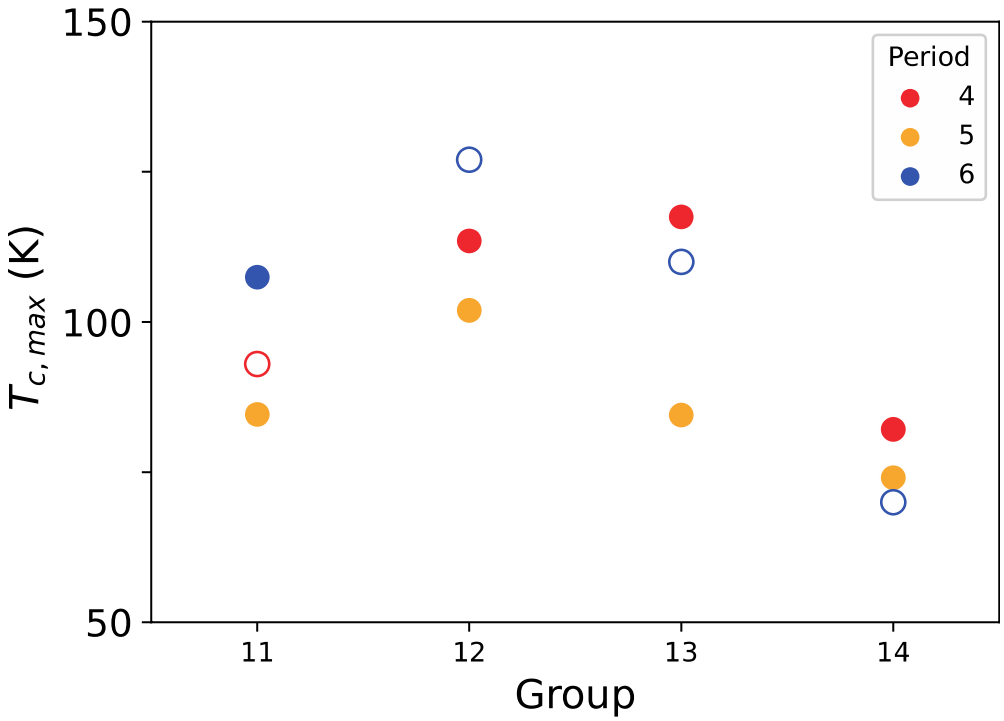

Figure S3. Calculated $T_{c,max}$ of hypothetical structures using the BFS 2C3F model (solid circles). The group 11 (Cu) of period 4, Group 12 (Hg), 13 (Tl), and 14 (Pb) of period 6 from the experimental $T_{c,max}$ (empty circles)[17,18,40,47]. The averaged values from the best three 2C3F models are used.

References

(1) Kresse, G.; Furthmüller, J. Efficient Iterative Schemes for Ab Initio Total-Energy Calculations Using a Plane-Wave Basis Set. *Phys. Rev. B* **1996**, *54* (16), 11169–11186.

(2) Perdew, J. P.; Burke, K.; Ernzerhof, M. Generalized Gradient Approximation Made Simple. *Phys. Rev. Lett.* **1996**, *77* (18), 3865–3868.

(3) Elfimov, I. S.; Sawatzky, G. A.; Damascelli, A. Theory of Fermi-Surface Pockets and Correlation Effects in Underdoped $YBa_2Cu_3O_{6.5}$. *Phys. Rev. B* **2008**, *77* (6), 060504(R).

(4) Kim, S.; Chen, X.; Fitzhugh, W.; Li, X. Apical Charge Flux-Modulated In-Plane Transport Properties of Cuprate Superconductors. *Phys. Rev. Lett.* **2018**, *121* (15), 157001.

(5) Uchida, S. *High Temperature Superconductivity The Road to Higher Critical Temperature*; Springer Japan: Tokyo, 2015; Ch. 3.5.

(6) You, D.; Ganorkar, S.; Kim, S.; Kang, K.; Shin, W.-Y.; Lee, D. Machine Learning-Based Prediction Models for Formation Energies of Interstitial Atoms in HCP Crystals. *Scr. Mater.* **2020**, *183*, 1–5.

(7) Kim, C.; Pilania, G.; Ramprasad, R. From Organized High-Throughput Data to Phenomenological Theory Using Machine Learning: The Example of Dielectric Breakdown. *Chem. Mater.* **2016**, *28* (5), 1304–1311.

(8) Ghiringhelli, L. M.; Vybiral, J.; Levchenko, S. V.; Draxl, C.; Scheffler, M. Big Data of Materials Science: Critical Role of the Descriptor. *Phys. Rev. Lett.* **2015**, *114* (10), 105503.

(9) Pilania, G.; Mannodi-Kanakkithodi, A.; Uberuaga, B. P.; Ramprasad, R.; Gubernatis, J. E.; Lookman, T. Machine Learning Bandgaps of Double Perovskites. *Sci. Rep.* **2016**, *6* (1), 19375.

(10) Breiman, L. Random Forests. *Mach. Learn.* **2001**, *45* (1), 5–32.

(11) Pedregosa, F.; Varoquaux, G.; Gramfort, A.; Michel, V.; Thirion, B.; Grisel, O.; Blondel, M.; Prettenhofer, P.; Weiss, R.; Dubourg, V.; *et al*. Scikit-Learn: Machine Learning in Python. *J. Mach. Learn. Res.* **2011**, *12*, 2825–2830.

(12) Torrance, J. B.; Bezinge, A.; Nazzal, A. I.; Huang, T. C.; Parkin, S. S. P.; Keane, D. T.; LaPlaca, S. J.; Horn, P. M.; Held, G. A. Properties That Change as Superconductivity Disappears at High-Doping Concentrations in $La_{2-X}Sr_xCuO_4$. *Phys. Rev. B* **1989**, *40* (13), 8872–8877.

(13) Cava, R. J.; Santoro, A.; Johnson, D. W.; Rhodes, W. W. Crystal Structure of the High-Temperature Superconductor $La_{1.85}Sr_{0.15}CuO_4$ above and below Tc. *Phys. Rev. B* **1987**, *35* (13), 6716–6720.

(14) Cava, R. J.; Santoro, A.; Krajewski, J. J.; Fleming, R. M.; Waszczak, J. V.; Peck, W. F.; Marsh, P. The Crystal Structure of the $La_{1.6}Sr_{0.4}CaCu_2O_{6\pm\delta}$ Superconductor. *Phys. C* **1990**, *172* (1–2), 138–142.

(15) Fuertes, A.; Obradors, X.; Navarro, J. M.; Gomez-Romero, P.; Casañ-Pastor, N.; Pérez, F.; Fontcuberta, J.; Miravitlles, C.; Rodriguez-Carvajal, J.; Martínez, B. Oxygen Excess and Superconductivity at 45 K in $La_2CaCu_2O_{6+y}$. *Phys. C* **1990**, *170* (1–2), 153–160.

(16) Zandbergen, H. W.; Fu, W. T.; van Ruitenbeek, J. M.; de Jongh, L. J.; van Tendeloo, G.; Amelinckx, S. Superconductivity in $(Pb, Bi)_2Sr_{2-x}La_xCu_2O_{6+\delta}$. *Phys. C* **1989**, *159* (1–2), 81–86.

(17) Subramanian, M. A.; Gopalakrishnan, J.; Torardi, C. C.; Gai, P. L.; Boyes, E. D.; Askew, T. R.; Flippen, R. B.; Farneth, W. E.; Sleight, A. W. Superconductivity near Liquid Nitrogen Temperature in the Pb-Sr-R-Ca-Cu-O System (R=Y or Rare Earth). *Phys. C*

1989, *157* (1), 124–130.

(18) Ohta, Y.; Tohyama, T.; Maekawa, S. Apex Oxygen and Critical Temperature in Copper Oxide Superconductors: Universal Correlation with the Stability of Local Singlets. *Phys. Rev. B* **1991**, *43* (4), 2968–2982.

(19) Jorgensen, J. D.; Veal, B. W.; Paulikas, a. P.; Nowicki, L. J.; Crabtree, G. W.; Claus, H.; Kwok, W. K. Structural Properties of Oxygen-Deficient $YBa_2Cu_3O_{7-\delta}$. *Phys. Rev. B* **1990**, *41* (4), 1863–1877.

(20) Grybos, J.; Hohlwein, D.; Zeiske, T.; Sonntag, R.; Kubanek, F.; Eichhorn, K.; Wolf, T. Atomic Displacements in the Ortho-II Phase of $YBa_2Cu_3O_{6.50}$ by Synchrotron X-Ray Diffraction. *Phys. C* **1994**, *220* (1–2), 138–142.

(21) Lindemer, T. B.; Chakoumakos, B. C.; Specht, E. D.; Williams, R. K.; Chen, Y. J. Effects of Composition and Processing on the Superconductivity of $La_{1+z}Ba_{2-z}Cu_3O_y$. *Phys. C* **1994**, *231* (1–2), 80–90.

(22) Guillaume, M.; Allenspach, P.; Henggeler, W.; Mesot, J.; Roessli, B.; Staub, U.; Fischer, P.; Furrer, A.; Trounov, V. A Systematic Low-Temperature Neutron Diffraction Study of the $RBa_2Cu_3O_x$ (R=yttrium and Rare Earths; X=6 and 7) Compounds. *J. Phys. Condens. Matter* **1994**, *6* (39), 7963–7976.

(23) Veal, B. W.; Paulikas, A. P.; Downey, J. W.; Claus, H.; Vandervoort, K.; Tomlins, G.; Shi, H.; Jensen, M.; Morss, L. Varied Oxygen Stoichiometry in $RBa_2Cu_3O_{7-x}$. *Phys. C* **1989**, *162–164*, 97–98. https://doi.org/10.1016/0921-4534(89)90935-0.

(24) Schnelle, W.; Braun, E.; Broicher, H.; Dömel, R.; Ruppel, S.; Braunisch, W.; Harnischmacher, J.; Wohlleben, D. Fluctuation Specific Heat and Thermal Expansion of YBaCuO and DyBaCuO. *Phys. C* **1990**, *168* (5–6), 465–474.

(25) Samoylenkov, S. V.; Gorbenko, O. Y.; Kaul, A. R. Superconducting Properties of Oxygen Deficient $LuBa_2Cu_3O_{7-x}$ Thin Films. *Phys. C Supercond.* **1996**, *267* (1–2), 74–78.

(26) Matskevich, N.; Wolf, T. Synthesis and Physico-Chemical Properties of Phase-Pure Ceramic $LuBa_2Cu_3O_{7-\delta}$. *Thermochim. Acta* **2008**, *467* (1–2), 113–116.

(27) Torardi, C. C.; McCarron, E. M.; Subramanian, M. A.; Horowitz, H. S.; Michel, J. B.; Sleight, A. W.; Cox, D. E. Structure-Property Relationships for $RBa_2Cu_3O_x$ Phases. *ACS Symp. Ser.* **1987**, *351*, 152–163.

(28) Harshman, D. R.; Mills, A. P. Concerning the Nature of High-Tc Superconductivity: Survey of Experimental Properties and Implication for interlayer coupling. *Phys. Rev. B* **1992**, *45* (18), 10684–10712.

(29) Asano, H.; Ishigaki, T.; Takita, K. Crystal Structure of the $HoBa_2Cu_3O_x$ Superconductor Determined by X-Ray Powder Diffraction. *Jpn. J. Appl. Phys.* **1987**, *26* (Part 2, No. 5), L714–L715.

(30) Stangl, E.; Proyer, S.; Borz, M.; Hellebrand, B.; Bäuerle, D. Pulsed-Laser Deposited $GdBaSrCu_3O_{7-\delta}$ and $GdBa_2Cu_3O_{7-\delta}$ Films. *Phys. C Supercond.* **1996**, *256* (3–4), 245–252.

(31) Guillaume, M.; Allenspach, P.; Henggeler, W.; Mesot, J.; Roessli, B.; Staub, U.; Fischer, P.; Furrer, A.; Trounov, V. A Systematic Low-Temperature Neutron Diffraction Study of the $RBa_2Cu_3O_x$ (R=yttrium and Rare Earths; x=6 and 7) Compounds. *J. Phys. Condens. Matter* **1994**, *6* (39), 7963–7976.

(32) Bernardi, E.; Lascialfari, A.; Rigamonti, A.; Romanò, L.; Scavini, M.; Oliva, C. Superconducting Diamagnetic Fluctuations in Sm-Based Underdoped Cuprates Studied via SQUID Magnetometry. *Phys. Rev. B* **2010**, *81* (6), 064502.

(33) Pavarini, E.; Dasgupta, I.; Saha-Dasgupta, T.; Jepsen, O.; Andersen, O. K. Band-Structure

Trend in Hole-Doped Cuprates and Correlation with *Tcmax*. *Phys. Rev. Lett.* **2001**, *87* (4), 047003.

(34) Torardi, C. C.; Subramanian, M. A.; Calabrese, J. C.; Gopalakrishnan, J.; McCarron, E. M.; Morrissey, K. J.; Askew, T. R.; Flippen, R. B.; Chowdhry, U.; Sleight, A. W. Structures of the Superconducting Oxides $Tl_2Ba_2CuO_6$ and $Bi_2Sr_2CuO_6$. *Phys. Rev. B* **1988**, *38* (1), 225–231.

(35) Miura, S.; Yoshitake, T.; Shohata, N.; Satoh, T. Dependence of Structural and Superconducting Properties of As-Grown $Bi_2Sr_2Ca_1Cu_2O_x$ Films on Low Temperature Annealing. *Phys. C* **1990**, *165* (3–4), 241–246.

(36) Hervieu, M.; Michel, C.; Domenges, B.; Laligant, Y.; Lebail, A.; Ferey, G.; Raveau, B. Electron Microscopy Study of the Superconductor "$Bi_2Sr_2CaCu_2O_{8+\delta}$." *Mod. Phys. Lett. B* **1988**, *02* (01), 491–500.

(37) Watanabe, T.; Fujii, T.; Matsuda, A. Structural Study of Inhomogeneous Charge Distribution of Inequivalent CuO_2 Planes in $Bi_{2.1}Sr_{1.9}Ca_2Cu_3O_{10+\delta}$ Single Crystals. *J. Phys. Soc. Japan* **2003**, *72* (11), 2924–2929.

(38) Lösch, S.; Budin, H.; Eibl, O.; Hartmann, M.; Rentschler, T.; Rygula, M.; Kemmler-Sack, S.; Huebener, R. P. Structural Analysis and Superconducting Properties of Pb-Free $Bi_2Sr_2Ca_3Cu_4O_y$ (n=4, Nominal Composition). *Phys. C Supercond.* **1991**, *177* (4–6), 271–280.

(39) Matheis, D. P.; Snyder, R. L. The Crystal Structures and Powder Diffraction Patterns of the Bismuth and Thallium Ruddlesden-Popper Copper Oxide Superconductors. *Powder Diffr.* **1990**, *5* (1), 8–25.

(40) Shimakawa, Y.; Kubo, Y.; Manako, T.; Igarashi, H. Variation in Tc and Carrier

Concentration in Tl-Based Superconductors. *Phys. Rev. B* **1989**, *40* (16), 11400–11402.

(41) Subramanian, M. A.; Calabrese, J. C.; Torardi, C. C.; Gopalakrishnan, J.; Askew, T. R.; Flippen, R. B.; Morrissey, K. J.; Chowdhry, U.; Sleight, A. W. Crystal Structure of the High-Temperature Superconductor $TI_2Ba_2CaCu_2O_8$. *Nature* **1988**, *332* (6163), 420–422.

(42) Parkin, S. S. P.; Lee, V. Y.; Engler, E. M.; Nazzal, A. I.; Huang, T. C.; Gorman, G.; Savoy, R.; Beyers, R. Bulk Superconductivity at 125 K in $Tl_2Ca_2Ba_2Cu_3O_x$. *Phys. Rev. Lett.* **1988**, *60* (24), 2539–2542.

(43) Cox, D. E.; Torardi, C. C.; Subramanian, M. A.; Gopalakrishnan, J.; Sleight, A. W. Structure Refinements of Superconducting $Tl_2Ba_2CaCu_2O_8$ and $Tl_2Ba_2Ca_2Cu_3O_{10}$ from Neutron Diffraction Data. *Phys. Rev. B* **1988**, *38* (10), 6624–6630.

(44) Chen, Z. Y.; Sheng, Z. Z.; Tang, Y. Q.; Li, Y. F.; Wang, L. M.; Pederson, D. O. Synthesis and Characterization of 2234-Phase $Ti_2Ba_2Ca_3Cu_4O_{12}$ Prepared near and at the Melting Point. *Supercond. Sci. Technol.* **1993**, *6* (4), 261–264.

(45) Ogborne, D. M.; Weller, M. T. The Structure of $Tl_2Ba_2Ca_3Cu_4O_{12}$. *Phys. C Supercond.* **1992**, *201* (1–2), 53–57.

(46) Putilin, S. N.; Antipov, E. V.; Chmaissem, O.; Marezio, M. Superconductivity at 94 K in $HgBa_2CuO_{4+\delta}$. *Nature* **1993**, *362* (6417), 226–228.

(47) Loureiro, S. M.; Antipov, E. V.; Tholence, J. L.; Capponi, J. J.; Chmaissem, O.; Huang, Q.; Marezio, M. Synthesis and Structural Characterization of the 127 K $HgBa_2CaCu_2O_{6.22}$ Superconductor. *Phys. C* **1993**, *217* (3–4), 253–264.

(48) Hunter, B. A.; Jorgensen, J. D.; Wagner, J. L.; Radaelli, P. G.; Hinks, D. G.; Shaked, H.; Hitterman, R. L.; Von Dreele, R. B. Pressure-Induced Structural Changes in Superconducting $HgBa_2Ca_{n-1}Cu_nO_{2n+2+\delta}$ (n = 1, 2, 3) Compounds. *Phys. C* **1994**, *221* (1–

2), 1–10.

(49) Antipov, E. V.; Abakumov, A. M.; Putilin, S. N. Chemistry and Structure of Hg-Based Superconducting Cu Mixed Oxides. *Supercond. Sci. Technol.* **2002**, *15* (7), R31–R49.

(50) Paranthaman, M.; Chakoumakos, B. C. Crystal Chemistry of $HgBa_2Ca_{n-1}Cu_nO_{2n+2+\delta}$ (n= 1, 2, 3, 4) Superconductors. *J. Solid State Chem.* **1996**, *122* (1), 221–230.

(51) Huang, Q.; Chmaissem, O.; Capponi, J. J.; Chaillout, C.; Marezio, M.; Tholence, J. L.; Santoro, A. Neutron Powder Diffraction Study of the Crystal Structure of $HgBa_2Ca_4Cu_5O_{12+\delta}$ at Room Temperature and at 10 K. *Phys. C Supercond.* **1994**, *227* (1–2), 1–9.